Materials Horizons

ROYAL SOCIETY OF CHEMISTRY

COMMUNICATION

View Article Online
View Journal

Check for updates

Cite this: DOI: 10.1039/d0mh00853b

Received 24th May 2020,
Accepted 29th June 2020

DOI: 10.1039/d0mh00853b

rsc.li/materials-horizons

A 3D nm-thin biomimetic membrane for ultimate molecular separation†

Tongshuai Wang,‡[ab] Siwei Liang,‡[a] Zhen Qi,[a] Monika Biener,[a] Thomas Voisin,[a] Joshua A. Hammons,[a] Ich C. Tran,[a] Marcus A. Worsley,[a] Tom Braun,[a] Y. Morris Wang,[a] Juergen Biener,[a] Theodore Baumann,[a] Sangil Kim *[b] and Jianchao Ye *[a]

Multi-functional membranes with high permeance and selectivity that can mimic nature's designs have tremendous industrial and bio-medical applications. Here, we report a novel concept of a 3D nanometer (nm)-thin membrane that can overcome the shortcomings of conventional membrane structures. Our 3D membrane is composed of two three-dimensionally interwoven channels that are separated by a continuous nm-thin amorphous TiO_2 layer. This 3D architecture dramatically increases the surface area by 6000 times, coupled with an ultra-short diffusion distance through the 2–4 nm-thin selective layer that allows for ultrafast gas and water transport, ~900 l m^{-2} h^{-1} bar^{-1}. The 3D membrane also exhibits a very high ion rejection (R ~ 100% for potassium ferricyanide) due to the combined size- and charge-based exclusion mechanisms. The combination of high ion rejection and ultrafast permeation makes our 3DM superior to the state-of-the-art high-flux membranes whose performances are limited by the flux-rejection tradeoff. Furthermore, its ultimate Li^+ selectivity over polysulfide or gas can potentially solve major technical challenges in energy storage applications, such as lithium–sulfur or lithium–O_2 batteries.

New concepts

Highly permeable and selective membranes are immensely desired for a wide range of applications, such as dialysis, water purification, and energy storage. However, conventional synthetic membranes based on two-dimensional (2D) structures suffer from the trade-off limitation between permeability and selectivity, arising from their intrinsically limited surface area and long tortuous pore geometries. Biological systems achieve a highly selective and rapid transmembrane mass transport by employing efficient three-dimensional (3D) functional structures. Inspired by the glomerular structure in the kidneys, here we report a self-supportive 3D membrane composed of two 3D interconnected channels which are separated by a nm-thin porous TiO_2 layer. This unique bio-mimetic 3D architecture drastically enlarges the effective filtration area, while its extremely thin selective layer provides an ultra-short diffusion distance. These features provide the 3D membrane's high separation performance with fast mass-transfer characteristics. Our study suggests that the 3D membrane has great potential for overcoming the limitations of conventional synthetic membranes. In addition, the results of this work provide fundamental design criteria for the development of high-performance nanoporous membranes.

Introduction

The ultimate goal in membrane design is to combine high permeability and high selectivity.[1–4] Nature solved this challenge by developing complex three-dimensional (3D) functional membrane architectures that provide organs, like the kidneys, liver, lungs, and intestinal villi, with unique functionalities. For example, the formation of urine is a process that begins with glomerular filtration in the kidneys. On average, in a 70 kg adult, the glomerular filtration rate is about 180 L day^{-1} of glomerular filtrate. At a hydrostatic pressure of <2 psi the high filtration rate is enabled by a unique 3D membrane morphology comprising a bundle of capillaries with a 645 cm^2 filtration area per 100 cm^2 of projected area (left panel of Fig. 1a).[5] Conventional approaches for the fabrication of high performance synthetic membranes, however, are still based on two-dimensional (2D) flat-sheet structures with single-functional pores, a design which suffers from the trade-off relationship between permeability and selectivity. In recent years, the development of ultra-thin membranes has attracted much attention;[6–8] this design strategy increases the overall flux by shortening the mass transport pathway. Atomic layer deposition (ALD), with atomic precision thickness, high conformality and uniformity, has also been an active research field for membrane applications.[9,10] However, the surface area of 2D membranes is intrinsically limited, not to mention the high probability of membrane failure due to the limited mechanical stability of ultra-thin membrane structures. To

---

[a] *Materials Science Division, Lawrence Livermore National Laboratory, Livermore, CA 94550, USA. E-mail: ye3@llnl.gov*

[b] *Department of Chemical Engineering, University of Illinois, Chicago, IL 60607, USA. E-mail: sikim@uic.edu*

† Electronic supplementary information (ESI) available. See DOI: 10.1039/d0mh00853b

‡ These authors contributed equally to this work.

address this shortcoming, rippled nanofilm geometries were designed to increase the surface area and hence improve the permeance.[11,12] However, the ripples in these membrane structures were not self-supportive, which limits the extent of increase in the surface area that can be achieved by this approach.

Inspired by the glomerular structure, we have developed a self-supportive 3D nm-thin membrane (3DM) with a well-defined architecture that offers extremely high filtration area combined with a nm-thin selective layer and a low tortuosity transport pore morphology for fast mass transport (right panel of Fig. 1a). Specifically, we use a templating approach to transform the characteristic bi-continuous ligament-pore morphology of nanoporous gold (np-Au) into a morphology consisting of two independent, interwoven mesopore channels that resembles the morphology of nature's 3DMs. In previous work, we have used this approach to fabricate nanotubular metal oxide foams.[13,14] In this work, we first sputter deposit a dense gold layer on one side of the np-Au disc. The purpose of the one-sided Au sputter coating is to provide access to the inside of the nanotubular pores while blocking the original pores of npAu on this side of the disk-shaped sample after the 3DM is generated by the following coating–etching steps. The actual membrane material is deposited by atomic layer deposition (ALD) which generates uniform and conformal metal oxide coatings with atom-scale thickness control. Finally, the np-Au template and the sputter coated Au layer are removed using a liquid etching process. This process generates the self-supportive 3DM morphology in which each tubular ligament is connected three-dimensionally with the adjacent ligaments, resulting in excellent stiffness and strength,[13,14] and extraordinary separation performance.

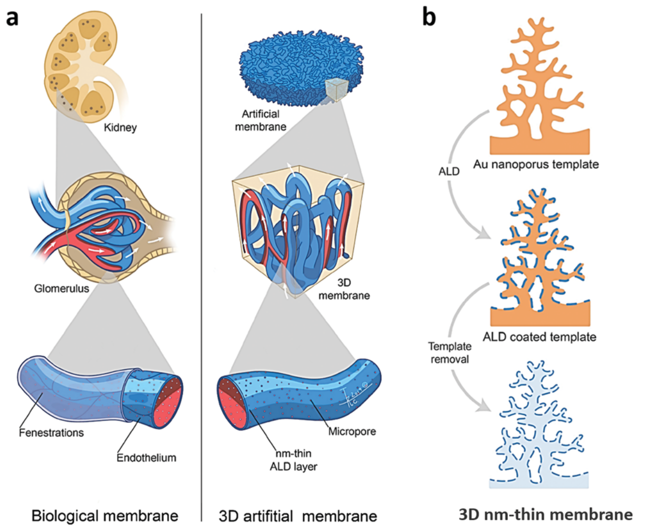

Fig. 1 Conceptional designs and fabrication schematics. (a) Morphological schematics of glomerulus filtration in the kidneys and the 3D membrane. (b) 2D illustrations of the 3D nm-thin membrane fabrication from nanoporous gold templating and atomic layer deposition (ALD) approach. The fabrication details can be found in the ESI.†

Results and discussion

Fabrication and morphology of 3DM

The fabrication process of 3DM is shown in Fig. 1b. Detailed information can be found in the Methods section. As illustrated in Fig. 1b and evidenced in Fig. 2a, both the inner and outer tubular channels of 3DM are three dimensionally self-connected and separated by a thin, porous TiO_2 layer, resulting in a gyroid-like membrane morphology that ensures no closed spaces or voids in the membrane structures. For the 3DM applications, it is critical that only one of the two independent pore systems can be accessed from each side of the disk shaped 3D-membrane. Here, we call the side opened to the outer tubular channel as the positive side (left panel of Fig. 2a), while the other side that is open to the inner tubular channel is called the negative side (right panel of Fig. 2a). Although pinholes cannot be theoretically excluded, high resolution scanning electron microscope (SEM) and aberration-corrected high-resolution transmission electron microscope (TEM) (Fig. 2b and c) analyses did not detect any large-sized pinhole or structural defects. Fig. 2d shows the pore size distribution measured using a N_2 desorption isotherm. The pore size around 50 nm is attributed to the diameter of the inner and outer tube channels inherited by the np-Au template. The micropores below 2 nm are attributed to pores in the TiO_2 ALD layer, which exhibit a size distribution between 0.4–0.8 nm and 1.1–1.7 nm. The existence of sub-nm pores in amorphous TiO_2 is expected due to the fluctuations of the local bonding conditions.[15,16] In order to explain the relationship between the TiO_2 layer structure and pore size, we employed small-angle X-ray scattering (SAXS) analysis based on a concentric cylinder shell model (Fig. 2e).[17] The results confirm that the ALD layer thickness only varies by 6% throughout the 200 μm-thick sample (see ESI† and Fig. S1 and S2). The χ^2 obtained from the SAXS model can be improved by introducing heterogeneous electron density fluctuations (in the order of ~1 nm) in the ALD layer by simulated annealing. While only heterogeneity normal to the wall surface can be accounted for in the SAXS modeling, the size of the fluctuations in Fig. 2e is in good agreement with the microporosity observed in the N_2 desorption experiments. The one-side volume-specific surface area of a 4 nm-thin TiO_2 3DM is 3.0×10^4 m^2 L^{-1}, as determined using the Brunauer–Emmett–Teller (BET) analysis, which is larger than the surface area of the corresponding np-Au template (2.3×10^4 m^2 L^{-1}). The extra 7000 m^2 L^{-1} surface area may be attributed to the micropores within the ALD layer. The surface area for the entire 200 μm-thick sample is 6000 times larger than the footprint area, which greatly enhances the mass transport through the 3D ALD layer. In order to evaluate the separation performance of the 3DM, we conducted gas and water permeance, and ion rejection tests under controlled conditions (*e.g.*, pressure- and diffusion-driven flows) that are relevant to their prospective applications, such as water purification, hemodialysis, and separators for energy conversion and storage.

Gas permeance

The gas permeance through a 2 nm-thin 3D TiO_2 membrane as a function of the inverse square root of the molecular weight, M_w, shows a nearly linear relationship (Fig. 3a). Only H_2 shows

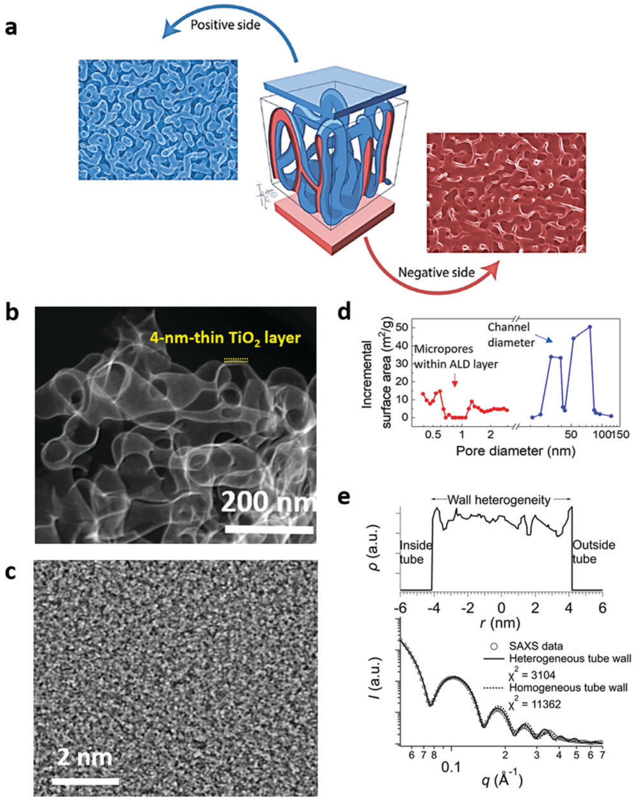

Fig. 2 Morphological and pore size characterizations. (a) SEM images of the positive side (blue) and the negative side (red) of the 3DM. (b) High-resolution transmission electron microscopy (HRTEM) image of the 3D membrane. (c) Aberration-corrected HRTEM image of an amorphous TiO_2 selective layer. (d) Mesopore size distributions (blue) calculated using Barrett–Joyner–Halenda (BJH) methods and micropore size distributions (red) based on density functional theory (DFT). The split of the peak around 50 nm is due to the channel size difference as the np-Au used here has a 70% porosity, making the outer tube channel larger than the inner tube channel. (e) Log–log plot of the background subtracted SAXS data (grey circles) with the least squares fit of a narrow size-distribution of hollow cylinders with a homogenous shell (dashed line) and a heterogeneous shell obtained by simulated annealing of the electron density within the shell (solid line). The scattering length density of the heterogeneous shell wall obtained by simulated annealing is shown in the top graph.

a small offset from this linear relationship. This suggests that gas transport through our 3DM is mainly dominated by Knudsen diffusion where the mean free path of gas molecules is larger than the pore width. A H_2 permeance of 3.4×10^{-5} mol m^{-2} s^{-1} Pa^{-1} is achieved with a H_2/CO_2 separation factor of 6.09. The measured separation factor is higher than that predicted by Knudsen diffusion (4.69), thus implying an enhanced interaction of H_2 with TiO_2.[18,19] The H_2 permeance of the 3DM is at least one order of magnitude higher than other sub-nm pore membranes (*e.g.* silica,[20,21] graphene[22]) or mesoporous membranes,[21] owing to the exceedingly high surface area and ultra-thin selective layer (inset in Fig. 3a).

Ion separation and water permeance

Water permeation rates through the 3DM were measured using two different methods: a pressure-driven flow and an osmotic pressure method. In the pressure-driven flow test, external pressure (6 psi) was directly applied to a home-made filtration cell.[23–25] The water permeation rate under the external pressure was found to be ~1260 L m^{-2} h^{-1} bar^{-1} (calculated based on the footprint-based surface area). For the osmotic pressure method, the water flux of the 3D nm-thick membrane was measured using a home-made diffusion cell fabricated by 3D printing. 1030 mg L^{-1} of DB71 solution was used as the drawing solution to generate an osmotic pressure gradient (0.35 psi). Using UV-vis spectroscopy we found that not even trace amounts of DB71 were present in the permeation solution after 48 hours of measurement, indicating the complete rejection of DB71. In contrast, a TiO_2 coated np-Au sample with only positive channels accessible on both sides of the membrane (generated by omitting the one-sided Au sputter-coating in the 3DM fabrication process) showed only 84% DB71 rejection with a permeance of 250 L m^{-2} h^{-1} bar^{-1}. This indicates that the diffusion through the thin ALD TiO_2 selective layer is critical for achieving the high ion rejection properties of the 3DM. Since the membrane has a high rejection towards DB71, the change of the osmotic pressure caused by the diffusion of DB71 is negligible. As shown in Fig. S3, ESI,† the dye solution level in the left reservoir increases quickly, and the membrane shows a water permeance of 892 L m^{-2} h^{-1} bar^{-1}. The difference in the water permeation rates measured by two different methods is presumably attributed to the presence of a concentration polarization of DB71 on the membrane surface which can reduce the water flux through the membrane.

We evaluated the ionic separation properties of our 3DM through filtration experiments using different types of dyes and ions based on a common test method for research-level nanoporous membranes described in many other works.[26–32] Fig. 3b and Table S1, ESI† show the molecular sieving properties of the 4 nm-thin 3DM for NaCl, $MgSO_4$, potassium ferricyanide (PFCN), ruthenium-tris(2,2′-bipyridyl)dichloride (Rubypy), Direct Blue 71 (DB71), and Congo red (CR). The 3DM showed a high rejection performance, >90%, for ions with hydrated radii larger than 3.7 Å. NaCl rejection (86%) is lower than that of $MgSO_4$ (~100%), which has been observed in many other membranes.[33–35] From the BET measurement, the average pore size in the ALD layer (1.1 nm) is smaller than the molecular dimensions of DB71 and CR, implying that the higher rejection rate for these dye molecules could be attributed to the size exclusion effects.[36] However, 3DM exhibited a high rejection rate of ~100% for PFCN and $MgSO_4$, although their hydrated diameters are smaller than the pore size in the ALD layer, while a slightly lower rejection rate of 95.63% was observed for Rubypy. Thus, the selective ion/molecular transport through our 3DM seems to be influenced by other factors, such as electrostatic interactions between membrane surface and charged species.

To further investigate the effect of surface charges on the ion selectivity of our 3DM, we measured the zeta potential (Fig. S4, ESI†) revealing an iso-electrical point (IEP) around pH 4 and suggesting a negatively charged membrane surface at pH = 7. The estimated surface charge density is 8.389×10^{-3} C m^{-2} which is close to the value reported in the literature.[37] Due to

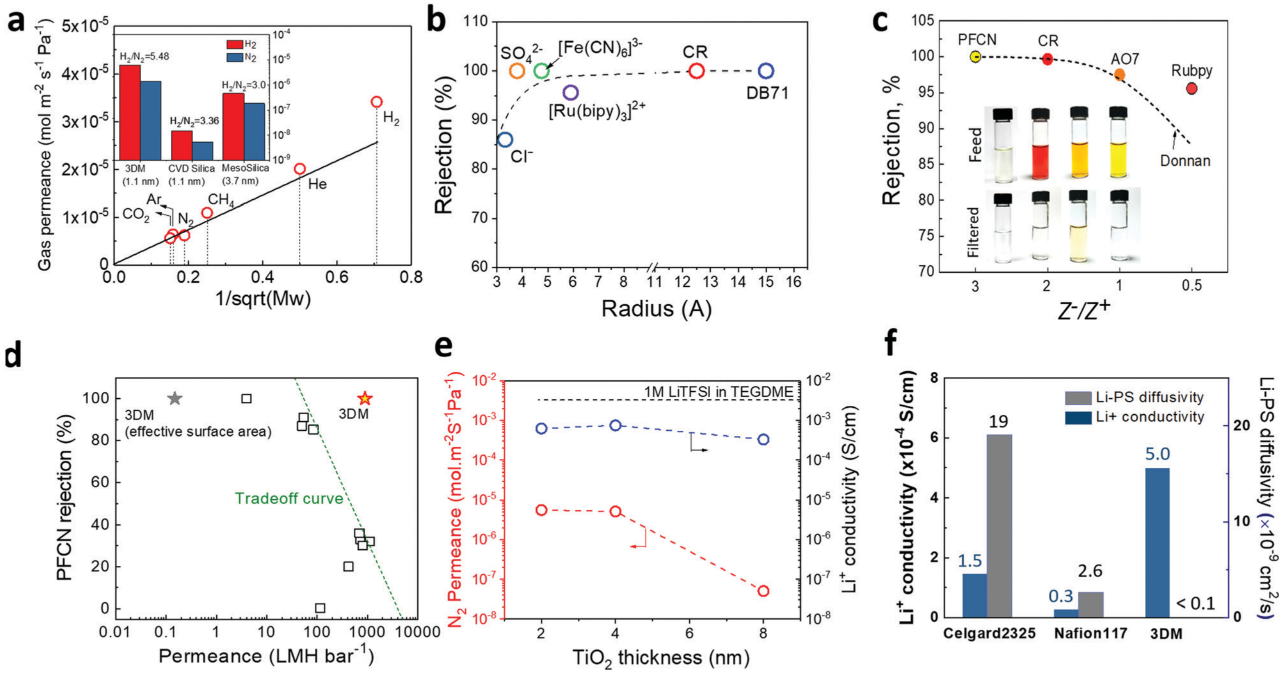

Fig. 3 Separation properties. (a) Gas permeance as a function of inverse square root of molecule weight. Inset shows H_2/N_2 selectivity (on the top of bar graph) and H_2 permeance (right *y*-axis) of the 3DM compared to the 1.1 nm-pore size CVD microporous silica membrane and the 3.7 nm-pore size mesoporous silica membrane. (b) Experimental ion and dye rejection ratio of a 4 nm-thin 3DM as a function of the molecule's hydrated radius. (c) Rejection ratio of ions with different valences and estimation from the Donnan exclusion model. (d) Comparison of water permeance and PFCN separation performance of the 3DM with the other state-of-the-art membranes. All the permeance values except the gray color star symbol are based on the projected area. Detailed information on other high flux membranes is available in the ESI,† Fig. S5 and Table S2. (e) N_2 permeance and Li^+ conductivity of 3DMs with varied TiO_2 thickness. (f) Li^+ conductivity and Li-PS diffusivity values of Celgard 2325, Nafion 117, and the 3DM. Li-PS diffusivity was evaluated by using UV-vis spectroscopy.

the electrostatic interactions, the Donnan potential on the membrane/solution interface tends to exclude co-ions, which gives a higher rejection rate for the negatively charged ions.[29] The estimated Debye length (λ_D) in the presence of 0.1 mM PFCN is 12.4 nm, greater than the micropore size of 3DM. Therefore, the high rejection rate for PFCN seems to be mainly due to the electrostatic repulsion given by the negative surface charge of our 3DM, similar to observations in sub-2 nm carbon nanotube pores.[29] Another important consequence of the Donnan exclusion is the dependence of the rejection rate on the ratio of the valency of the anion ($z-$) and cation ($z+$), as suggested by eqn (S1) in the ESI.† This is supported by the fact that our 3DM shows a slightly lower rejection rate for AO7 and Rubypy, which has the $z-/z+$ ratio of 1 and 0.5, respectively, lower than that of the other negatively charged molecules, PFCN (3) and CR (2). Therefore, we could conclude that the high rejection rates of 3DM against charged species is a combined effect of charge and size of the molecules.

In Fig. 3d, Fig. S5 and Table S2, ESI,† we compare the PFCN separation performance of our 3DM with other high flux membranes reported so far, including a nanostrand-channelled graphene oxide (NSC-GO) membrane (691 L m^{-2} h^{-1} bar^{-1}), and a WS_2 nanosheet membrane (750 L m^{-2} h^{-1} bar^{-1}).[32,38] It is important to note that the NSC-GO membrane and WS_2 membrane showed only 36% and 33% rejections for PFCN ions, compared to ~100% for our 3DM. Our 3D membrane combines a very high ion rejection and a water permeance of 1260 L m^{-2} h^{-1} bar^{-1} (calculated based on the footprint-based surface area) and thus outperforms all other high flux membranes. Note, that its separation performance is far beyond the trade-off curve for PFCN rejection and water permeance. Although all permeance values of other membranes in Fig. 3d are based on the projected area of the membranes, we also include the permeance of our 3DM based on the effective surface area (gray color star symbol). If the effective membrane surface area of the 3DM is employed to calculate the permeance value, it is only ~0.15 L m^{-2} h^{-1} bar^{-1}, which is 6000 times lower than that calculated from the projected area. Thus, we conclude that the overall high permeance of the 3DM originates from its high internal surface area.

Our 3DMs could also be used for Li–O_2 and Li–S battery applications. Different from the N_2 permeance, the Li^+ conductivity is insensitive to the ALD TiO_2 thickness (Fig. 3e). The fast transport of Li^+ through our 3DM is attributed to the smaller ionic radius (76 pm) compared to the micropores in the TiO_2 layer. In addition, our 3DM exhibits the infinitesimal permeation of polysulfide (S_8^{2-}), while offering a high Li^+ conductivity. The Li^+ conductivity over polysulfide blocking ability of our 3DM is significantly better than that of Celgard® 2325, a conventional battery separator, and Nafion®, a benchmark ion exchange membrane (Fig. 3f). Therefore, it seems to be possible to develop 3DMs that allow selective Li^+ transport

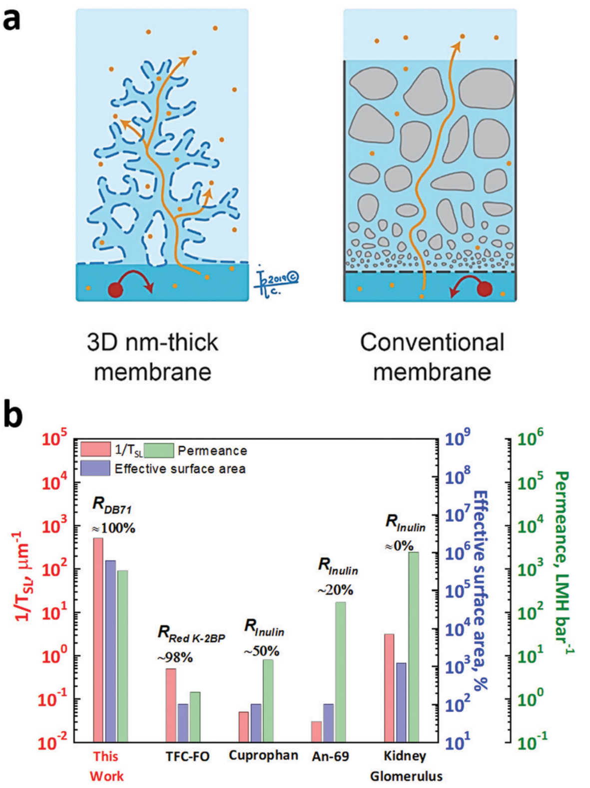

Fig. 4 Membrane morphology and performance relationship. (a) Schematics of the selective transport of molecules and ions through the biomimetic structure of the 3DM (left), and the conventional synthetic membrane pore structure (right). (b) Comparison of the reported value for the active surface area and the reciprocal of selective layer thickness ($1/T_{SL}$) of a biological membrane, and commercial and lab-fabricated osmosis membranes to those obtained in this study.

while blocking larger molecules such as O_2 (M_w close to N_2) or lithium polysulfides (Li_2S_n, n = 2–8). Such membranes would solve the critical degradation issues of Li–O_2 and Li–sulfur batteries related to O_2 crossover and Li_2S_n shuttling.[39]

Understanding the high selectivity and permeance

We attribute the remarkable selectivity and permeance of our 3DM to its unique bicontinuous pore morphology and the ultra-thin selective layer (Fig. 1a and 4a). The interconnected channels provide continuous pathways for fast mass transport towards the membrane surface throughout the volume of our 3DM. Meanwhile, the thin TiO_2 ALD selective layer, with a high surface area and micropore density, and a small pore size, functions as an ideal barrier to separate small molecules or ions by size and charge-induced exclusions with a very low transport resistance, as described in Table S3 and Fig. S6, ESI.† Indeed, experimental and calculation results indicate that the resistance of the long tubular mesoporous channels is higher than that of the thin TiO_2 layer by several orders of magnitude. If the large surface area of the TiO_2 layer would be hypothetically unfolded onto a flat plane, the actual areal permeance of the 4 nm-thick TiO_2 layer would be 0.15–0.21 L m^{-2} h^{-1} bar^{-1}, which is a relatively small value for such a thin membrane. For example, it has been reported that 26-nm-thick and 450 nm-thick TiO_2 membranes exhibited water permeance values of 7 and 33 L m^{-2} h^{-1} bar^{-1}, respectively.[40,41] Thus, our calculation suggests that the mass transfer rate of our 3DM is impaired to a certain extent by the long and tortuous inner and outer tubular channels that can be optimized in future work.

As shown in Fig. 4a, in contrast to our 3DM, the mass transfer and separation efficiencies of the conventional synthetic membrane systems are limited by the long-range mass transport pathway and low surface area. To better elucidate how the structure characteristics of membranes affect their mass transport rates, we calculated the effective surface area (ESA) based on the ratio of the selective surface area over footprint area (see ESI† for details). The 200 μm-thick 3DM presents an ESA (600 000%) higher than biological membranes (645%)[42,43] and conventional synthetic membranes (~100%)[44–46] by three orders of magnitude, which is highly consistent with the experimentally observed ultrafast mass transport of our 3DMs. Fig. 4b provides a more insightful interpretation on the relationship between the structure and separation performance of our 3DM compared to biological (glomerulus) filtration,[47] synthetic dialysis (Curophan and An-69[44,45]), and thin-film composite forward osmosis membranes (TFC-FO[46]). We used direct blue 71 (DB71, 3 × 1.5 × 1 nm of molecular dimension[48]) for our 3DM to properly compare the separation performances of other membranes from the literature that used Red K-2BP (~1.8 nm of diameter calculated using Chem3D) or inulin (~2.8 nm of diameter[47]). In both the synthetic and biological membranes, membranes with a higher ESA or $1/T_{SL}$ show a higher water permeance because membrane permeance is directly proportional to its surface area and inversely proportional to its thickness. Water permeance of the glomerulus filtration in the kidneys is higher than that of commercial dialysis membranes and TFC-FO by several orders of magnitude while it is not able to exclude inulin due to its large molecular weight cut-off (MWCO) ranging from 30 to 50 kDa (4.1–4.8 nm of Stokes diameter). The TFC-FO shows a high rejection value for the Red K-2BP; however, its permeance is the smallest due to its nonporous dense selective layer compared to other synthetic porous membranes. Although the pore size of our 3DM is around 1.1 nm, it outperforms all the compared membranes in permeance and in rejection due to its large surface area and its nm-thin membrane wall with combined molecular sieving and charge-based exclusion. These unique structural and surface properties provide our 3D nm-thin bio-mimic membranes with both excellent ion rejection rates and ultra-fast water transport properties, which can offer a figure of merit for membrane performance for various practical applications.

Conclusions

We have developed self-supportive biomimetic 3D membranes with orders of magnitude larger surface area than the footprint area and a nanometer thin separating layer. High mass transport rates and excellent selectivity were observed in gas, water, and ion permeance experiments. Our 3DM also exhibits promising applications in the energy storage area, for instance, as a membrane for Li–S and Li–O_2 batteries. Our current approach using nanoporous gold as a sacrificial template suffers from the high material costs of gold and the large transport resistance associated with the unimodal size distribution of the transport pores inherited from npAu. While npAu is an ideal template for demonstrating our 3D membrane technology approach, it is important to note that other, less expensive templates such as npCu[49] or 3D printed polymer[50] templates are readily available. The size of micropores in the ALD TiO_2 layer can be manipulated by deposition temperature and chemistry. High temperature leads to denser and more crystalline structures and therefore smaller sub-nm pores. The micropore size may also be adjusted by modifying the ALD process chemistry by using other ALD precursors (various metal oxides and metals), doping with other atoms, multilayer deposition, *etc.* By adopting machine learning based architectural optimizations and additive manufacturing techniques, both the mechanical and transport properties of future 3DMs can be further improved. Different coating materials such as ductile metals and elastic polymers can also be developed to replace metal oxides to meet specific servicing environments. Surface modification with anti-fouling functional groups or the development of a hierarchical porous template with a low tortuosity can reduce fouling of organic substances on the 3DM surface. It can be envisioned that these 3DMs will have broad applications in biomedical engineering (*e.g.*, hemodialysis) and many other diffusion-based membrane separations (*e.g.* forward osmosis, catalysis, energy conversion and storage).

Experimental

Fabrication of 3D membranes

A sheet of $Ag_{70}Au_{30}$ alloy was cut into ~200 μm thick discs with 1/4 inch diameter. The disc samples were annealed at 900 °C in air for 12 h before being dealloyed using concentrated nitric acid at room temperature for 48 h. A higher annealing temperature than those of the previous reports[13,14] increases the grain size and improves the quality of the grain boundaries, which significantly mitigates the grain boundary over-etching issue during dealloying and reduces the corresponding defects. The resulting nanoporous discs were washed with deionized water and dried in air. Thereafter, a thin layer of gold (approximate 500 nm) was sputtered onto one side of the discs to close the positive pore channel on one side of the nanoporous gold discs and to open the negative pore channel at a later stage (Fig. 1b). Then nanometer thick Al_2O_3 and TiO_2 films were deposited onto the nanoporous gold templates (middle panel of Fig. 1b) by ALD using the well-established trimethyl-aluminum ($AlMe_3/H_2O$) and titanium tetrachloride ($TiCl_4/H_2O$) ALD processes in a warm wall reactor (wall and stage temperature of 125 °C for Al_2O_3 and 110 °C for TiO_2) on a ALD-200L system (Kurt J. Lesker Company). Long pump, exposure, and purge times (20/300/300 s) were used to ensure that the gas precursors penetrate through the np-Au discs and achieve uniform coatings. The Al_2O_3/gold and TiO_2/gold samples were immersed into a mixture of 2 g KI, 1 g I_2, 2 g H_2O, 8 g acetone and 8 g ethanol for 48 h to completely remove the sacrificial gold template (bottom panel of Fig. 1b). The smaller amount of H_2O used in this etching recipe reduces the chemical damage to the ALD coating. The additional freestanding 2D ALD film on the sealing Au layer will peel off automatically, leaving the inner tubular channel opened on this side, which we note as the negative side (right panel of Fig. 2a). Finally, the discs were rinsed with acetone and super critically dried to afford semitransparent 3D membranes of Al_2O_3 or TiO_2.

Structural, morphological, and compositional characterizations

The morphology of the 3D membranes was characterized using a field emission scanning electron microscope (JEOL 7401-F) at 20 keV (20 mA) in secondary electron imaging mode with a working distance of 5–8 mm. Transmission electron microscopy (TEM) was conducted using a Philips CM300 FEG system. Specific surface area and pore size distributions were analyzed using nitrogen adsorption/desorption isotherms using Brunauer–Emmett–Teller (BET), Barret-Joyner-Halenda (BJH), and density functional theory (DFT) methods, with an ASAP 2020 surface area analyzer (Micromeritics Instrument Corp.). We note that this porosity analysis cannot detect pore sizes smaller than the diameter of the N_2 molecule itself (3.64 Å).

Small angle X-ray scattering (SAXS) modeling

In order to resolve the wall thickness and heterogeneity, SAXS experiments were conducted in the q-range: $0.05\ \text{Å}^{-1} < q < 2.5\ \text{Å}^{-1}$. Only data out to $q = 0.7\ \text{Å}^{-1}$ were analyzed using the small angle scattering theory, which can resolve scattering heterogeneities between 1 nm and 12 nm.[51] The SAXS experiments were performed at the advanced light source, beamline 7.3.3 using monochromatic X-rays with a wavelength of 1.2398 Å and a beam area of 0.3 mm by 0.7 mm. The as-prepared TiO_2 membranes were placed in the beam such that the entire membrane thickness was oriented normal to the X-ray beam path. Only the electron density fluctuations on the length scales associated with the TiO_2 wall were resolved, while the size of the inner and outer tube radii (~50 nm) and the overall fibrous network (100 s of nm) were not; these dimensions would only be accessible by scattering at lower q. Detailed SAXS analysis and modeling can be found in the ESI.†

Zeta potential measurements and surface charge calculations

The zeta potential was measured using the streaming current method on a SurPASS 3 electrokinetic analyzer (Anton Paar GmbH, Graz, Austria). The sample size is 10 mm × 20 mm. A 1 mM KCl electrolyte was used for the measurement. The electrolyte was purged with nitrogen for 10 minutes prior to the measurement and during the entire measurement to prevent the dissolution of CO_2. A pH scan measurement was performed beginning at pH 5.5 (pH of fresh 5 mM KCl) and ramped down to pH 3 by the addition of 0.05 M HCl. The zeta potential was determined at roughly every 0.5 pH units after the sample was rinsed for 5 minutes using the pH adjusted electrolyte. A basic pH ramp was then performed by following the exact same procedure as above. The pH, in this case, was adjusted by the addition of 0.05 M NaOH.

Membrane characterization

Gas and water transport properties of the 3DM were characterized using the methods described in our previous studies.[23,24,52] To investigate the intrinsic transport properties of the membrane, we used freestanding 3DM with a thickness of 200–400 μm and a diameter of ~6 mm (*d*/*t* aspect ratios of 15 to 30). The disc was mounted on a polyester film with a 1/4" diameter hole and Torr-seal epoxy was used to seal the edge. No other membrane supporting materials below the 3DM surface were used. This setup allows the accurate measurement of the actual sample area for uniform mass flow without resistance from the membrane support but limits the maximum applied pressure as deflection of the membrane will cause cracking along the edges of the membrane disc.

For the evaluation of gas permeance, the flux of gas through the 3D membrane was measured using a constant pressure system equipped with a calibrated digital mass flow meter. In these tests, the high pressure side was the negative side of the 3DM (Fig. 2a) and the flow rate through the 3DM towards the positive side was measured. To evaluate whether there is any viscous flow through any large pinholes or large structural defects, N_2 permeance of the 3DM was measured at several different pressures by increasing pressure from 0.1 to 10 psi. After the 3DM showed independency on the applied pressure, other gases such as H_2, He, CH_4, Ar, and CO_2 were tested.[24]

For the evaluation of the dye molecule/ion rejection, typical ion rejection tests for the characterization of the nanoporous membranes were carried out using a home-made filtration cell as described in detail elsewhere.[23,24] Low-concentration electrolyte solutions were used throughout this study to ensure that the Debye length (λ_D) was large enough so that a complete double-layer overlap could be achieved within the nanochannels. For the pressure driven-flow test, 2 mL of the feed solution (*e.g.* 100 mg L^{-1} of PFCN) was pressurized at 10 psi with a controlled nitrogen gas line, while the permeate was at atmospheric pressure. After the permeation of 200 μL of the solution through the membrane, permeate solutions were collected for UV-analysis.[23,24]

For the osmotic pressure method, an osmotic water flux measurement cell was 3D printed (Form 2 printer, Formlabs, Somerville, MA, USA). Each cell comprises a chamber in connection with a square-shape capillary tube (0.25 cm^2 cross-section area), as shown in Fig. S3, ESI.† At the beginning of the measurement, 10.0 mL of 1030 mg L^{-1} (1 mM) DB71 dye and deionized water were filled in the feed side and permeate side of the cell, respectively. The solutions at both sides of the cell were mixed continually using magnetic stirrers to reduce external concentration polarization. At the initial stage, the solution in the capillary tube in both cells was at the same level. The volume change in both cells was calculated by measuring the difference of the solution level at designated time intervals. The concentration of the dye in both cells was measured using UV-vis spectroscopy at the same time interval to correct for changes in the osmotic pressure difference caused by the change of concentration over time. The increase of the difference of the solution level can result in the change in pressure difference across the membrane, which was taken into consideration for the calculation of the osmotic water permeance.[53]

In the diffusion set-up for the Donnan exclusion test, a 10 mL solution with a dye/ion concentration of 0.1 mM was filled in the feed side of the cell and the same amount of DI water was filled in the permeate side of the cell (PermeGear, Inc. USA). The solution in each cell was continually mixed using magnetic stirrers. The collected permeate solutions were analyzed subsequently using UV-1800 ultraviolet-visible spectrophotometer (Shimadzu. Japan) to determine the concentration of the ions. The permeability of the ions was calculated by linearly fitting the concentration in the permeation solution with time. The detailed UV-vis spectroscopy data can be found in Fig. S7, ESI.†

For the polysulfide permeation test, the polysulfide permeability across the membrane samples was evaluated by using a diffusion cell inside an argon-filled glovebox. The feed solution consisting of Li_2S_8 was dissolved in a 1 : 1 volume mixture of 1,3-dioxolane (DOL) and dimethyl ether (DME), which was prepared by reacting stoichiometric amounts of Li_2S with sulfur at 70 °C for 24 hours. The feed side reservoir was initially filled with Li_2S_8 of 3380 mg L^{-1} solution and the permeate side reservoir was filled with the same amount of DOL/DME solution. A magnetic stirrer was placed in each cell and stirring was continued during the test to avoid concentration polarization. The polysulfide concentration at the permeant side was monitored using UV-vis spectroscopy. The testing samples were sealed carefully in a UV quartz cuvette with Teflon screw cap and septum, and then quickly transferred to a UV chamber for testing. The PS permeability through the membrane was calculated from Fick's law:

$$V\frac{\mathrm{d}C_\mathrm{p}(t)}{\mathrm{d}t} = A\frac{P}{L}\left(C_\mathrm{f} - C_\mathrm{p}(t)\right)$$

where V is the volume of solution, C_f and C_p is the PS concentration in the feed and permeate, respectively, t is time, A is area, P is permeability, and L is membrane thickness. The UV-vis has *ca.* 3 mg L^{-1} of measurement resolution for lithium polysulfides (Li_2S_8) and the lowest permeability that can be determined for Li_2S_8 is approximately 0.92×10^{-10} cm^2 s^{-1} in this study. We observed no UV-vis signal for Li_2S_8 in the permeate solution.

Li^+ conductivity

Li^+ conductivities of the 3DMs with varying ALD TiO_2 layer thicknesses were measured by placing them in between two Li metal electrodes with fixed spacing. 1 M Lithium bis(trifluoromethanesulfonyl)imide (LiTFSI) in Tetraethylene glycol dimethyl ether (TEGDME) was used as the liquid organic electrolyte. Electrochemical impedance spectroscopy (EIS) was recorded using a VSP-300 multichannel potentiostat (Bio-Logic Science Instruments). The solution and contact resistances were removed as background to obtain the resistance from the 3DMs.

Conflicts of interest

There are no conflicts to declare.

Acknowledgements

The work was performed under the auspices of the US Department of Energy by LLNL under Contract No. DE-AC52-07NA27344. The project was supported by the Laboratory Directed Research and Development (LDRD) program of LLNL (13-LWD-031, 16-ERD-051), and the Institutional Scientific Capability Portfolio (ISCP) investments. S. Kim and T. Wang acknowledge financial support from the National Science Foundation (Grant No. CBET-1706910). J. Ye acknowledges Anton Paar GmbH for zeta potential measurements.

Notes and references

1 A. Lee, J. W. Elam and S. B. Darling, *Environ. Sci.: Water Res. Technol.*, 2016, **2**, 17–42.

2 M. Vinoba, M. Bhagiyalakshmi, Y. Alqaheem, A. A. Alomair, A. Pérez and M. S. Rana, *Sep. Purif. Technol.*, 2017, **188**, 431–450.

3 D. R. Dekel, *J. Power Sources*, 2018, **375**, 158–169.

4 Y. Shi, C. Eze, B. Xiong, W. He, H. Zhang, T. Lim, A. Ukil and J. Zhao, *Appl. Energy*, 2019, **238**, 202–224.

5 A. Bohle, B. Aeikens, A. Eenboom, L. Fronholt, W. R. Plate, J.-C. Xiao, A. Greschniok and M. Wehrmann, *Kidney Int.*, 1998, **54**, S186–S188.

6 J. Zhao, Q. Deng, A. Bachmatiuk, G. Sandeep, A. Popov, J. Eckert and M. H. Rümmeli, *Science*, 2014, **343**, 1228–1232.

7 H. W. Kim, H. W. Yoon, S.-M. Yoon, B. M. Yoo, B. K. Ahn, Y. H. Cho, H. J. Shin, H. Yang, U. Paik and S. Kwon, *Science*, 2013, **342**, 91–95.

8 H. Li, Z. Song, X. Zhang, Y. Huang, S. Li, Y. Mao, H. J. Ploehn, Y. Bao and M. Yu, *Science*, 2013, **342**, 95–98.

9 M. Weber, A. Julbe, A. Ayral, P. Miele and M. Bechelany, *Chem. Mater.*, 2018, **30**, 7368–7390.

10 H.-C. Yang, R. Z. Waldman, Z. Chen and S. B. Darling, *Nanoscale*, 2018, **10**, 20505–20513.

11 S. Karan, Z. W. Jiang and A. G. Livingston, *Science*, 2015, **348**, 1347–1351.

12 Z. Tan, S. Chen, X. Peng, L. Zhang and C. J. S. Gao, *Science*, 2018, **360**, 518–521.

13 J. Ye, A. C. Baumgaertel, Y. M. Wang, J. Biener and M. M. Biener, *ACS Nano*, 2015, **9**, 2194–2202.

14 M. M. Biener, J. Ye, T. F. Baumann, Y. M. Wang, S. J. Shin, J. Biener and A. V. Hamza, *Adv. Mater.*, 2014, **26**, 4808–4813.

15 H. Zhang, B. Chen, J. F. Banfield and G. A. Waychunas, *Phys. Rev. B: Condens. Matter Mater. Phys.*, 2008, **78**, 214106.

16 J. Ye, P. Shea, A. C. Baumgaertel, S. A. Bonev, M. M. Biener, M. Bagge-Hansen, Y. M. Wang, J. Biener and B. C. Wood, *Chem. Mater.*, 2018, **30**, 8871–8882.

17 I. Livsey, *J. Chem. Soc., Faraday Trans.*, 1987, **83**, 1445–1452.

18 M. M. Islam, M. Calatayud and G. Pacchioni, *J. Phys. Chem. C*, 2011, **115**, 6809–6814.

19 K. Sun, M. Kohyama, S. Tanaka and S. Takeda, *J. Phys. Chem. C*, 2014, **118**, 1611–1617.

20 R. M. de Vos and H. Verweij, *Science*, 1998, **279**, 1710–1711.

21 X. Gao, J. C. D. da Costa and S. K. Bhatia, *J. Membr. Sci.*, 2013, **438**, 90–104.

22 S. Huang, M. Dakhchoune, W. Luo, E. Oveisi, G. He, M. Rezaei, J. Zhao, D. T. Alexander, A. Züttel and M. S. Strano, *Nat. Commun.*, 2018, **9**, 2632.

23 F. Fornasiero, J. Bin In, S. Kim, H. G. Park, Y. Wang, C. P. Grigoropoulos, A. Noy and O. Bakajin, *Langmuir*, 2010, **26**, 14848–14853.

24 S. Kim, F. Fornasiero, H. G. Park, J. Bin In, E. Meshot, G. Giraldo, M. Stadermann, M. Fireman, J. Shan, C. P. Grigoropoulos and O. Bakajin, *J. Membr. Sci.*, 2014, **460**, 91–98.

25 J. K. Holt, H. G. Park, Y. Wang, M. Stadermann, A. B. Artyukhin, C. P. Grigoropoulos, A. Noy and O. Bakajin, *Science*, 2006, **312**, 1034–1037.

26 L. Sun, H. Huang and X. Peng, *Chem. Commun.*, 2013, **49**, 10718–10720.

27 X. Peng, J. Jin, Y. Nakamura, T. Ohno and I. Ichinose, *Nat. Nanotechnol.*, 2009, **4**, 353.

28 W. Hirunpinyopas, E. Prestat, S. D. Worrall, S. J. Haigh, R. A. Dryfe and M. A. Bissett, *ACS Nano*, 2017, **11**, 11082–11090.

29 F. Fornasiero, H. G. Park, J. K. Holt, M. Stadermann, C. P. Grigoropoulos, A. Noy and O. Bakajin, *Proc. Natl. Acad. Sci. U. S. A.*, 2008, **105**, 17250–17255.

30 J. K. Holt, A. Noy, T. Huser, D. Eaglesham and O. Bakajin, *Nano Lett.*, 2004, **4**, 2245–2250.

31 J. K. Holt, H. G. Park, Y. Wang, M. Stadermann, A. B. Artyukhin, C. P. Grigoropoulos, A. Noy and O. J. S. Bakajin, *Science*, 2006, **312**, 1034–1037.

32 L. Sun, Y. Ying, H. Huang, Z. Song, Y. Mao, Z. Xu and X. Peng, *ACS Nano*, 2014, **8**, 6304–6311.

33 Y.-C. Chiang, Y.-Z. Hsub, R.-C. Ruaan, C.-J. Chuang and K.-L. Tung, *J. Membr. Sci.*, 2009, **326**, 19–26.

34 Y. Zhang, S. Zhang and T.-S. Chung, *Environ. Sci. Technol.*, 2015, **49**, 10235–10242.

35 L. Ouyang, R. Malaisamy and M. L. Bruening, *J. Membr. Sci.*, 2008, **310**, 76–84.

36 C. C. Striemer, T. R. Gaborski, J. L. McGrath and P. M. Fauchet, *Nature*, 2007, **445**, 749.

37 K. C. Akratopulu, C. Kordulis and A. Lycourghiotis, *J. Chem. Soc., Faraday Trans.*, 1990, **86**, 3437–3440.

38 H. Huang, Z. Song, N. Wei, L. Shi, Y. Mao, Y. Ying, L. Sun, Z. Xu and X. Peng, *Nat. Commun.*, 2013, **4**, 2979.

39 Y. Yang, G. Zheng and Y. Cui, *Chem. Soc. Rev.*, 2013, **42**, 3018–3032.

40 X. Huang, C. Tian, H. Qin, W. Guo, P. Gao and H. Xiao, *Ceram. Int.*, 2020, **46**, 4679–4689.

41 S. Wu, Z. Wang, S. Xiong and Y. Wang, *J. Membr. Sci.*, 2019, **578**, 149–155.

42 J. Nyengaard and T. Bendtsen, *Anat. Rec.*, 1992, **232**, 194–201.

43 A. Ruggiero, C. H. Villa, E. Bander, D. A. Rey, M. Bergkvist, C. A. Batt, K. Manova-Todorova, W. M. Deen, D. A. Scheinberg and M. R. McDevitt, *Proc. Natl. Acad. Sci. U. S. A.*, 2010, **107**, 12369–12374.

44 E. Klein, F. Holland, A. Donnaud, A. Lebeouf and K. Eberle, *J. Membr. Sci.*, 1977, **2**, 349–364.

45 R. Wendt, E. Klein, E. Bresler, F. Holland, R. Serino and H. Villa, *J. Membr. Sci.*, 1979, **5**, 23–49.

46 P. Zhao, B. Gao, Q. Yue, J. Kong, H. K. Shon, P. Liu and Y. Gao, *Chem. Eng. J.*, 2015, **273**, 316–324.

47 R. Chang, I. Ueki, J. Troy, W. Deen, C. R. Robertson and B. Brenner, *Biophys. J.*, 1975, **15**, 887–906.

48 T.-Z. Ren, Z.-Y. Yuan and B.-L. Su, *Colloids Surf., A*, 2007, **300**, 79–87.

49 J. Hayes, A. Hodge, J. Biener, A. Hamza and K. Sieradzki, *J. Mater. Res.*, 2006, **21**, 2611–2616.

50 L. R. Meza, S. Das and J. R. Greer, *Science*, 2014, **345**, 1322–1326.

51 A. Guinier and G. Fournet, *Small-angle scattering of X-rays*, Wiley, New York, 1955.

52 A. Pendse, S. Cetindag, M.-H. Lin, A. Rackovic, R. Debbarma, S. Almassi, B. P. Chaplin, V. Berry, J. W. Shan and S. Kim, *Small*, 2020, **15**, 1904590.

53 N. Y. Yip, A. Tiraferri, W. A. Phillip, J. D. Schiffman and M. Elimelech, *Environ. Sci. Technol.*, 2010, **44**, 3812–3818.